Gas-solid fluidized bed simulations using the filtered approach: Validation against pilot-scale experiments

Wenchao Yu [a], Pascal Fede [a,*], Mahdi Yazdanpanah [b], Benjamin Amblard [c], Florian Euzenat [b], Olivier Simonin [a]

[a] Institut de Mécanique des Fluides de Toulouse (IMFT), Université de Toulouse, CNRS, FR-31400 Toulouse, France
[b] Total, Research & Technology Gonfreville (TRTG), Harfleur 76700, France
[c] IFP Energies Nouvelles, BP3, Solaize 69360, France

HIGHLIGHTS

- The large-scale fluidized bed simulations are validated against PSRI experiments.
- A SGS drag model based on the filtered approach is used without any specific tuning.
- Gas-solid flows inside the fluidized bed with different gas velocities are characterized.
- Validation in this study is a critical step toward industrial-scale fluidized bed simulations.

GRAPHICAL ABSTRACT

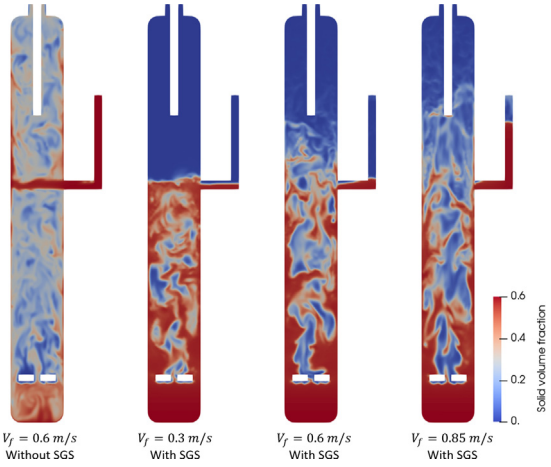

ARTICLE INFO

Keywords:
Fluidized bed
Subgrid scale drag
Euler-Euler approach
CFD

ABSTRACT

Numerical simulations of large-scale fluidized beds still remain challenging due to the computational limitation and experimental validation. In the present work, a CFD study of a large-scale fluidized bed is investigated using the NEPTUNE_CFD code based on an Eulerian n-fluid modeling approach. A SubGrid Scale (SGS) drag model based on the filtered approach is used to take into account the effect of very small solid structures unresolved with the coarse mesh. The numerical results are compared with the experimental data carried out in a pilot-scale cold-flow fluidized bed unit and provided by Particulate Solid Research Inc (PSRI). By applying the SGS drag model without any specific or empirical tuning, reasonably good grid-independence is achieved. The flow regimes inside the fluidized bed are well predicted for all the superficial gas velocities studied here. The bed density profiles and the solid entrainment fluxes are also in good agreement with the experimental measurement.

* Corresponding author.
E-mail address: pascal.fede@imft.fr (P. Fede).

https://doi.org/10.1016/j.ces.2020.115472.

1. Introduction

Thanks to the high efficiency of mixing, mass and heat transfer of the gas-solid fluidized beds, it has become an indispensable

equipment in many industrial applications, such as the fluid catalytic cracking (FCC) process in the petroleum refineries (Amblard et al., 2017). In order to optimize its design and improve its performance, the gas-solid fluidized bed has been widely studied in recent years. With the rapid development of the computational resources, CFD simulations have been used as a very important tool for the large-scale fluidized bed investigation. However, it has some specific challenges mainly related to the computation limitation and validation of the results. Even with HPC performances, the computational resources are still unaffordable for predicting the very small solid structures in the industrial-scale configurations using sufficiently fine grid. Therefore representative simulations of gas-solid fluidized bed on a coarse-grid is becoming a topic of great interest and challenge.

Igci and Sundaresan (2011a) and Parmentier et al. (2012) have reported that the simulations on the coarse-grid would result in a major overestimation of bed expansion or solid entrainment, which is related to the drag overestimation due to the effect of unresolved structures on the resolved flow. Various numerical methods and approaches to investigate and solve this problem have been well summarized and detailed in these reviews (van der Hoef et al., 2008; Wang, 2009; Schneiderbauer et al., 2013; Fullmer and Hrenya, 2017; Sundaresan et al., 2018).

According to Wang (2009), the empirical correlation or scaling factor methods were developed in the beginning, but they are only suitable for specific operating conditions and are difficult to be extended to other configurations. By assuming the important effect of the heterogeneous structures in the form of particle clusters, Energy Minimization Multi-Scale (EMMS) approach (Li and Kwauk, 1994; Li and Kwauk, 2003) was developed to calculate the structure-dependent drag coefficients, which was successful to predict the hydrodynamics of Geldart A particles in circulating fluidized bed (CFB) flows (Li et al., 2007; Wang et al., 2008).

A remarkable progress has been made in the last two decades for the filtered two fluid model (fTFM) which is derived from the spatial averaging of the kinetic theory based two fluid model (TFM) equations (Igci et al., 2008; Igci and Sundaresan, 2011a; Igci and Sundaresan, 2011b; Parmentier et al., 2012; Ozel et al., 2013; Milioli et al., 2013; Schneiderbauer and Pirker, 2014; Sarkar et al., 2016; Schneiderbauer, 2017; Cloete et al., 2018a; Cloete et al., 2018b), where the closure models are generally coming from the fine-grid TFM simulations. According to the budget analysis in Ozel et al. (2013), the SGS drag force has a dominant effect on the prediction of the bed expansion. Some recent studies (Milioli et al., 2013; Sarkar et al., 2016; Schneiderbauer, 2017; Cloete et al., 2018b) suggest that the other SGS terms such as the Reynolds-stress-like contribution will also be significant for the larger grid size simulations. Apparently, neglecting their contributions may change quantitatively the numerical prediction for some physical quantities, for example the rise velocity of bubbles is overestimated in Schneiderbauer et al. (2013). However, as observed in Schneiderbauer et al. (2013), the bed expansion (the bed density), the time-averaged solid volume fraction, the bubble size and its number density and the gas velocity can still be very well predicted in their study. This implies that neglecting the SGS stresses may have minor effect on the prediction of the bed expansion of the bubbling fluidized bed (Schneiderbauer, 2017; Cloete et al., 2018b) which confirms the budgets analysis in Ozel et al. (2013). As the actual study focus on the validation by comparing with experimental bed expansions, we choose to focus on the SGS drag force and to neglect the other SGS terms.

The correction given by the SGS drag models (Igci et al., 2008; Igci and Sundaresan, 2011b; Parmentier et al., 2012; Ozel et al., 2013; Schneiderbauer, 2017) depends strongly on the filter size $\overline{\Delta}$. This dependence is generally defined as $\overline{\Delta}^2/(\overline{\Delta}^2 + C)$, where C is a constant evaluated from the general information of the configurations, such as particle terminal settling velocity, particle relaxation time, acceleration of the gravity, bed hydraulic diameter etc., according to these studies (Igci et al., 2008; Igci and Sundaresan, 2011b; Parmentier et al., 2012; Schneiderbauer, 2017). But it is defined as a variable in the study of Ozel et al. (2013) where C depends on the local flow properties: the filtered particle relaxation time and the magnitude of the filtered relative velocity between gas and solid (Milioli et al., 2013; Sarkar et al., 2016). With the help of a dynamic adjustment procedure by applying a second filter (see in Appendix B and Parmentier et al. (2012)), the SGS drag model of Ozel et al. (2013) closed by the fine-grid simulations on the CFB flow can also well predict the hydrodynamics in a dense fluidized bed investigated in Parmentier et al. (2012) without any specific or empirical tuning, which shows certain universality.

To further show its applicability on the large-scale configuration in different flow regimes, the SGS drag model of Ozel et al. (2013) is used in the present work. The simulations are performed with NEPTUNE_CFD code which is based on an Eulerian n-fluid modeling approach. The results are validated with the experiments that were carried out in a pilot-scale cold-flow fluidized bed unit provided by PSRI. The experimental validation of this numerical study is a critical step toward full scale simulation of industrial fluidized bed units.

The paper is organized as follows: Sections 2 and 3 give the details about the experimental setup and numerical simulations, respectively. The mesh study in the absence of the SGS drag model is shown in Section 4. In Section 5, the effect of the SGS drag model is highlighted. The validation with different superficial gas velocities is presented in Section 6. Conclusions are drawn in Section 7.

2. Description of PSRI experiments

A number of experiments were performed by PSRI to measure the bubble properties (size, void fraction, frequency and velocity), solid circulation rate and bed density profiles in a 0.9 m diameter fluidized bed with Geldart Group A powders. More details are given below.

Tests were conducted in a 0.89 m inner diameter, 6.85 m tall steel fluidized bed unit shown in Fig. 1 (left), which contains three parts. The outlet on the top of the bed is connected by two cyclones to return the solid back to the bed. In Fig. 1 (right), an inside view of the test unit is presented. Fig. 1 (middle) shows the air distributor that is located at 0.82 m. The dipleg of the second cyclone has a part inside the bed, this leads to an annular shape for the bed outlet. According to the experimental observation, more than 99% of the entrained solids are returned into the bed through the dipleg of the first cyclone.

The experiments are operated with compressed dry air at ambient temperature at different superficial gas velocities varied from 0.3 to 0.85 m/s. The density and viscosity of air are 1.18 kg/m^3 and 1.85×10^{-5} Pa · s, respectively. The median size d_{p50} for the polydispersed particle is 78 μm with a density $\rho_p = 1490\ kg/m^3$. The total mass of solid particles inside the bed is estimated to 1815kg.

Two sets of experimental data are selected to validate our simulations. The first one is the vertical bed density profile along the height of the bed, which is measured using a set of pressure transmitters at the pressure ports located along the bed wall. The responses of these pressure transmitters were time averaged, normalized by the spacing between two ports (L) and the gravity g to give a vertical and localized bed density (DP/gL). The second one to be compared is the overall entrainment rate of solid particles from

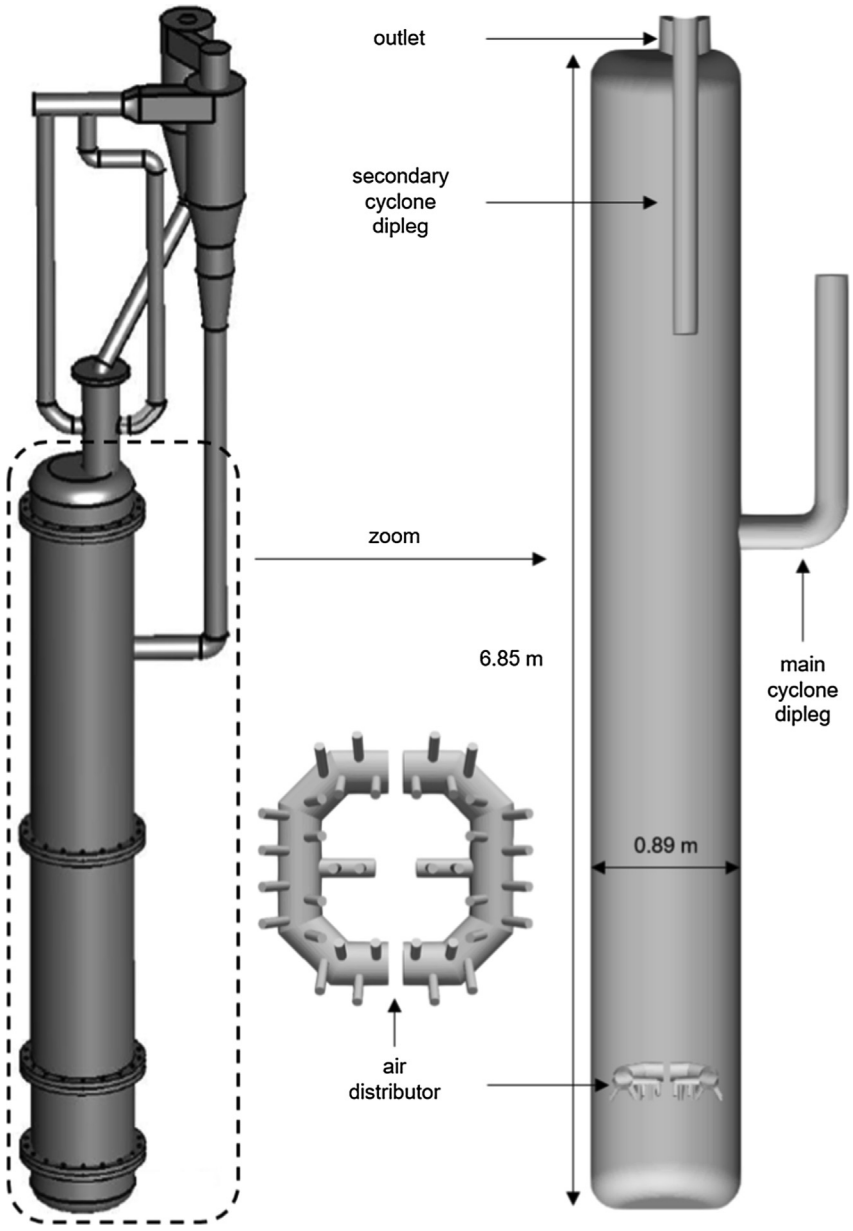

Fig. 1. Geometry of 0.9 m diameter fluidized bed of PSRI. Left: 3D model of the test unit, middle: air distributor and right: inside view of the test unit. Figures courtesy of PSRI.

the bed. It was measured by closing a pneumatically operated butterfly valve located in the first stage cyclone dipleg for thirty seconds.

3. Numerical simulation overview

The unsteady three dimensional numerical simulations of the fluidized-bed reactor were performed using the Eulerian N-fluid modeling approach for fluid-particle turbulent polydispersed reactive flows implemented in NEPTUNE_CFD V4.0.1@Tlse version by IMFT (Institut de Mécanique des Fluides de Toulouse). NEPTUNE_CFD is a computational multiphase flow software developed in the framework of the NEPTUNE project, financially supported by CEA (Commissariat á l'Énergie Atomique), EDF (Electricité de France), IRSN (Institut de Radioprotection et de Sûreté Nucléaire) and AREVA-NP. The approach is derived from a joint fluid-particle Probability Density Function (PDF) equation allowing to derive transport equations for the mass, momentum and agitation of particle phases. In the proposed modeling approach, transport equations (mass, momentum and fluctuating kinetic energy) are solved for each phase and coupled together through interphase transfer terms. For more details about the modeling approach and NEPTUNE_CFD, readers are invited to see reference papers (Fede et al., 2016; Gobin et al., 2003; Hamidouche et al., 2018; Simonin, 2000).

The SGS drag model developed by Parmentier et al. (2012) and Ozel et al. (2013) is used to take into account the effect of the unresolved solid structures that cannot be solved on a coarse grid. The idea is similar to the filter approach using in the Large Eddy Simulation in single-phase turbulent flow. A filter is applied to the transport equations. We assume that the filtered drag term can be split into a resolved part and an unresolved part. The unresolved part needs to be modeled using the resolved particle relaxation time and resolved particle and gas velocities. More details can be found in Appendix A, Parmentier et al. (2012) and Ozel et al. (2013). The model of Ozel et al. (2013) is used and validated with

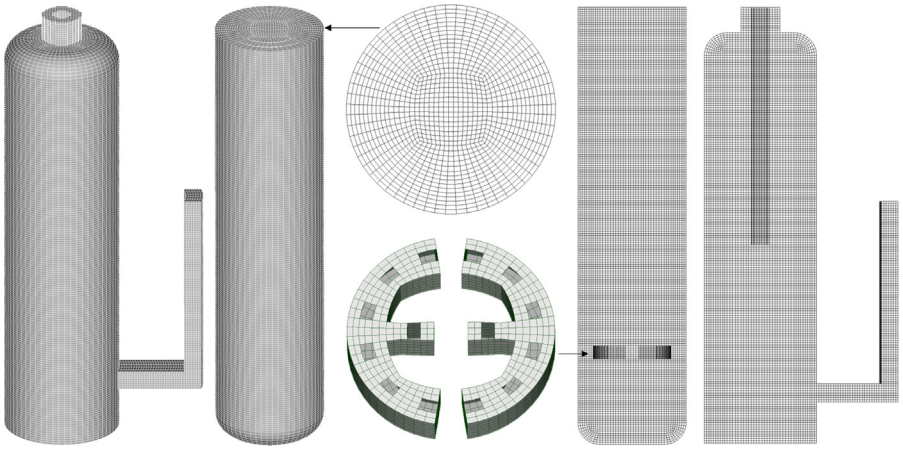

Fig. 2. Mesh with 424,563 cells. Left: mesh on the upper part of the bed body, middle-left: mesh on the lower part of the bed body, middle-top: O-grid mesh on a horizontal section of the bed, middle-bottom: mesh on the air distributor, middle-right: mesh on the lower part of a vertical plane and right: mesh on the upper part of a vertical plane.

the experimental results in this study. Fig. 2 shows the mesh on bed body, inside the bed and in the cross-section. Several simplifications have been made in order to use the structural mesh (hexahedral type). Compared to Fig. 1 (right), the dipleg of the second cyclone is shifted horizontally to the center of bed. The dipleg of the first cyclone is modeled by a square cross-sectional pipe. The nozzles of distributor are all neglected. The difference is less than 2% on the surface and volume after these simplifications.

As the nozzles of air distributor are neglected in the mesh, the inlet air is set to directly blow to the bed bottom, in other words the gas flow rate is imposed normal to the cell. A free pressure condition is used at the outlet. The solid mass flow rate at the outlet is re-injected by the dipleg, the solid volume fraction is imposed at 0.6. The internal dipleg is consider as dead-body. A friction wall boundary condition is used for the gas phase and a no-slip wall boundary condition is used for the solid phase. More details about the wall boundary condition of the solid phase can be found in Fede et al. (2016).

Only the monodisperse cases are introduced here with $d_p = d_{p50} = 78$ µm. According to the large particle to gas density ratio, the drag force is dominant for mean gas-particle interphase momentum transfer. The drag model of Gobin et al. (2003) has been used. Such a model is combination between the model proposed by Wen and Yu (1965) and the one proposed by Ergun (1952). For the gas phase we use $k-\varepsilon$ model with additional terms that take into account the effect of particles on gas turbulence, and the turbulent viscosity is also modified by the presence of solid phase. Particle agitation is modeled by the approach of two transport equations $q_p^2 - q_{gp}$, one for particle agitation, and another for gas-particle covariance. Collisions between particles are also taken into account and assumed uncorrelated (Simonin et al., 2002) and inelastic, particle-particle restitution coefficient is set to 0.9. Due to the presence of high solid volume fraction in the actual study, the frictional interaction between solid particles becomes very important and it is considered by adding a frictional part in the solid stress tensor in the momentum equation (Bennani et al., 2017), which was proposed by Srivastava and Sundaresan (2003) by modifying a rigid-plastic rheological model to account for strain rate fluctuations.

The numerical simulations are performed during 150 s of physical time. Flow inside the fluidized bed is established around at 30 s. It takes more time to achieve a balance on particle recycling through the cyclone dipleg with the increase of the superficial gas velocity. For the case $V_f = 0.85$ m/s, the solid surface in the cyclone dipleg maintains in a certain level from 60s. Then, the time-averaged statistics are computed from 60 s to the end of simulations (150 s).

4. Influence of mesh size

The influence of mesh size on the macroscopic behavior in the numerical simulations of fluidized beds has already been investigated (Agrawal et al., 2001; Igci et al., 2008; Parmentier et al., 2012; Ozel et al., 2013). It is also closely investigated in this study regarding its vital role in industrial modeling where mesh size tends to be large due to scale effect. The SGS drag model mentioned in the Section 3 was developed to be able to reduce the impact of mesh size and can help to accurately predict the mean properties in the fluidized beds. In order to demonstrate the need to use the SGS drag model in this study, three meshes are generated and some details of these meshes are given in the Table 1. The SGS drag model is considered as not necessary if a mesh-independent result can be achieved within the reasonable computational cost for an industrial use.

Results of the simulations on different mesh sizes without the SGS drag model are presented here with the superficial gas velocity $V_f = 0.6$ m/s. Fig. 3 shows the instantaneous solid volume fraction on the central plane. As the increase in the number of cells, a better resolution is obtained and finer structures can be observed. However, solid particles are still blown to all over the fluidized bed due to the overestimation of the drag force and nearly homogeneous particle distribution is formed for all the three meshes used

Table 1
Some details of meshes used in this study.

Number of cells	Typical cell size Δ (mm)	$\frac{\Delta}{d_p}$	Stokes relaxation time τ_p^{st} (s)	$\frac{\Delta}{(\tau_p^{st})^2 \|g\|}$
91,613	30 ∼ 40	385	0.028	3.91
424,563	18 ∼ 25	231	0.028	2.34
1,737,736	11 ∼ 16	141	0.028	1.43

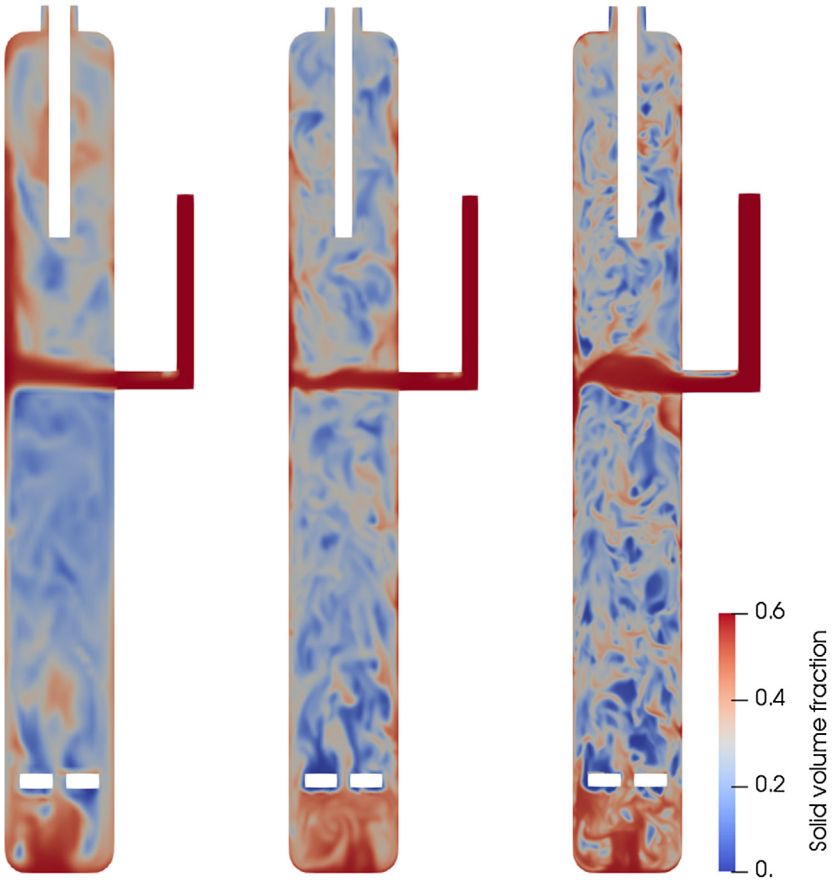

Fig. 3. Instantaneous solid volume fraction on different mesh sizes without the SGS drag model. Left: 91,613 cells, middle: 424,563 cells and right: 1,737,736 cells.

here. Due to the too large solid circulating rate, a jet is formed at the dipleg of the main cyclone and hits directly the opposite wall.

Quantitatively, the mean vertical bed density profiles are compared to the experimental measurements in Fig. 4. The bed density was calculated from pressure drops measured along the height of the bed wall. From the experimental data, we know that the bed was separated into two regions, a dense region with a bed density close to 700 kg/m^3 and a dilute region (free board) with very low solid concentration. The numerical results obtained with these meshes are failed to capture the desired flow regime, a circulating bed is predicted and the jump at 3 m above the air distributor corresponds to the jet returned by the dipleg.

The solid mass flow rates at the bed outlet are presented in Fig. 5. Corresponding to previous analysis, the solid fluxes oscillate between 100 and 500 kg/s. By reducing mesh size, a slight

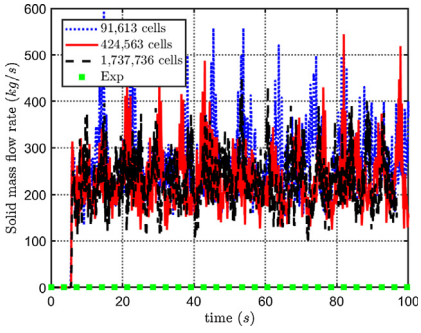

Fig. 5. Comparison of experimental and predicted solid mass flow rate at the outlet versus time (s) on different mesh sizes without the SGS drag model.

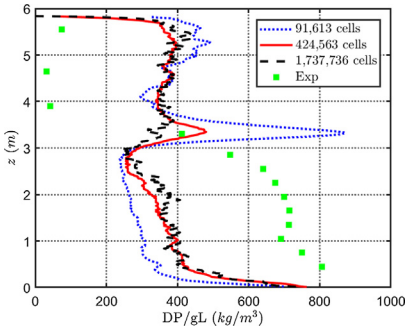

Fig. 4. Profiles of mean vertical bed density on different mesh sizes without the SGS drag model.

decrease of the time-averaged solid mass flow rate is observed, but it is still much higher than the experimental measurement which is 0.77 kg/s with $V_f = 0.6$ m/s. Through these simulations, even with the finest mesh used here (1,737,736 cells), numerical results are still away from the experimental data, which suggests to refine again the mesh size. According to Andrews et al. (2005), a mesh-independent solution could be obtained using a mesh size less than 10 particle diameters, which corresponds to around 5 billions cells for the actual cases. It exceeds the reasonable computational cost for a lab-scale gas-solid fluidized bed simulation. This issue is even more critical in case of industrial scale simulations where the bed size is more than 1 order of magnitude bigger than the pilot plant used in this study. Therefore, the SGS drag model is needed to overcome this problem.

5. Effect of the SGS drag model

The simulations with $V_f = 0.6$ m/s are re-performed on three different mesh sizes in the presence of the SGS drag model. Fig. 6 shows the instantaneous solid volume fraction. The effect of the SGS drag model is obviously observed, particle distributions are no longer homogeneous in the whole domain for the simulations on all the three meshes. A dense region is formed in the lower half of the fluidized bed while a dilute region is observed in the upper half. Meanwhile, less particles are entrained to the top region of the bed so that the solid mass flow rate decreases also at the bed outlet. More importantly, although the finer structures are resolved with the decrease of the mesh size, almost the same bed expansions are achieved for these three cases. It seems that reasonably good mesh-independent results are obtained in the presence of the SGS drag model.

These observations are confirmed quantitatively by Figs. 7 and 8. Compared to the cases without the SGS drag model, the mean vertical bed density profiles in Fig. 7 are much more improved and fit now to the experimental results. Meanwhile, the solid mass flow rates at the bed outlet in Fig. 8 decrease dramatically to the range between 0.4 and 1.3 kg/s, very close to experimental measurement 0.77 kg/s. Moreover, results between two finer meshes are closer to each other, this seems to indicate that the simulations with the SGS drag model tend to converge towards a result independent of the mesh. However, the solid mass flow rate is underpredicted compared to the experimental measurement. This underestimation may be related to three possible factors: i) the solid mass in the bed used in the simulation is underestimated compared to the experimental holdup; ii) the neglect of the poly-

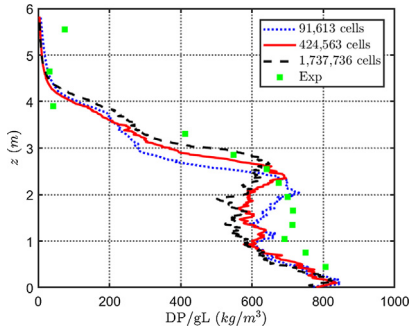

Fig. 7. Profiles of mean vertical bed density for different mesh sizes with the SGS drag model.

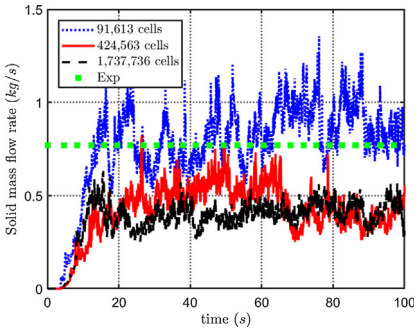

Fig. 8. Solid mass flow rate at the outlet versus time (s) for different mesh sizes with the SGS drag model.

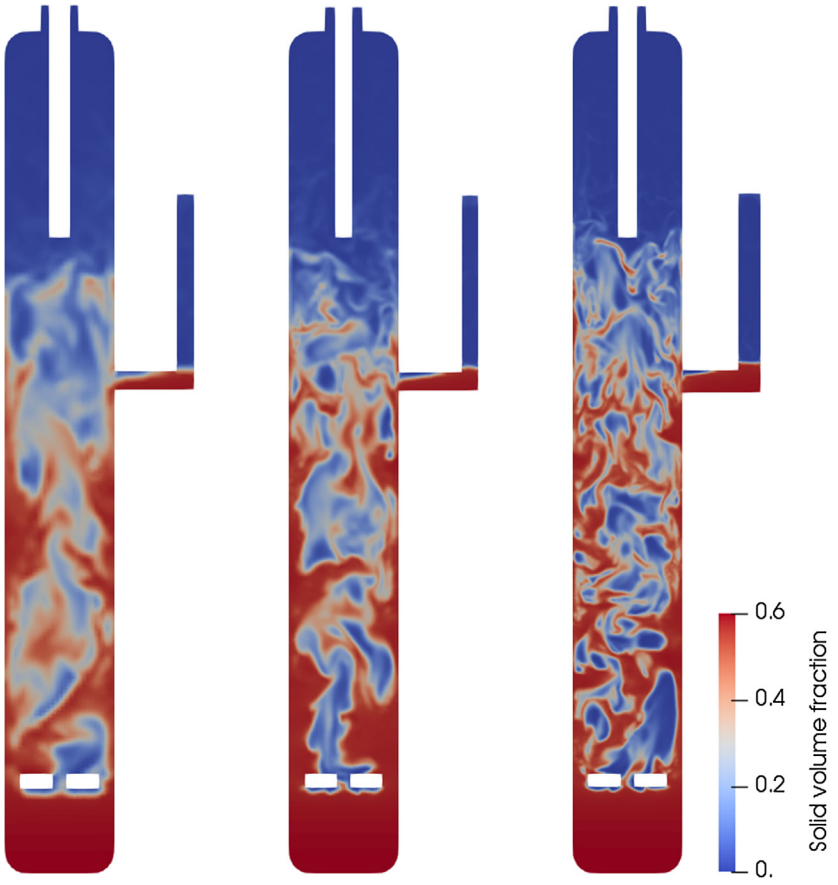

Fig. 6. Instantaneous solid volume fraction for different mesh sizes with the SGS drag model. Left: 91,613 cells, middle: 424,563 cells and right: 1,737,736 cells.

disperse effect; iii) the neglect of contributions from the other SGS terms, such as the SGS stresses (Milioli et al., 2013; Sarkar et al., 2016; Schneiderbauer, 2017; Cloete et al., 2018b).

In terms of the computational resources consumption for these three cases, it takes around 24,400 CPU hours for the case with mesh of 1,737,736 cells for running 150 s physical time, that corresponds roughly to 3 days of computational time on 360 cores, while it takes only 3,430 CPU hours for the mesh of 424,563 cells and 140 CPU hours for the mesh of 91,613 cells. Thus, the mesh with 424,563 cells has been selected for the following studies as a good compromise between the flow resolution and computational cost.

6. Superficial gas velocities

6.1. Validation

The simulations are performed for different superficial gas velocities $V_f = 0.3$, 0.6 and 0.85 m/s in the presence of the SGS drag model. Fig. 9 shows the instantaneous solid volume fractions. Bed expansion is enhanced with the increase of superficial gas velocity. With $V_f = 0.3$ m/s, a dense fluidized bed is obtained, particles rarely escape from the bed outlet. Increasing the superficial gas velocity to 0.6 m/s, as mentioned in the previous section, two regimes exist, one dense regime in the lower part and one dilute regime in the upper part. A small quantity of particles can fly up to the bed outlet and recycles through the main cyclone dipleg. Increasing again to $V_f = 0.85$ m/s, the expanded bed height can reach the lower part of the secondary cyclone dipleg, a circulating fluidized bed is nearly formed, particles are going to fill the cyclone dipleg.

In Fig. 10 (left), a very similar trend is observed compared to experimental bed density profiles for three superficial gas velocities. Bed densities in dense region are underestimated for all three cases as shown in Fig. 10 (right), 11% for the case of $V_f = 0.3$ m/s, 8% for $V_f = 0.6m/s$ and 2% for $V_f = 0.85$ m/s. It should be noted that the total mass of solid particles in the bed used in these simulations is only an estimation of mass computed from experimental density profiles. In addition, the bed holdup is a dynamic value which depends on the operating conditions. Therefore obtaining a precise value from experimental results in not possible. Considering the case of $V_f = 0.3$ m/s as an example, the difference of 87.5 kg/m^3 for the bed density between the numerical prediction and the experimental measurement in the dense region could make a difference of around $140kg$ for particle mass estimation. Hence, one reason of the underestimation of the bed density may come from the difference of the total solid mass used in the simulations and experiments. Moreover, assuming that the solid mass in the entire system was kept constant for all experiments, one would expect the solid holdup in the reactor would decrease with increasing fluidization velocity. If accounting for this variation in the reactor holdup in the simulations (instead of using a fixed holdup for all three cases here), it should negate the trend that the simulations tend to increasingly underestimate the bed density with lowering fluidization velocity observed in Fig. 10 (right).

In Fig. 11, the solid mass flow rates at the bed outlet are presented and compared with experimental results. Considering the influences from the mass estimation problem mentioned in the previous paragraph and the monodisperse assumption, it is totally acceptable to have a predicted solid mass flow rate slightly underestimated but still rested in the same order of magnitude

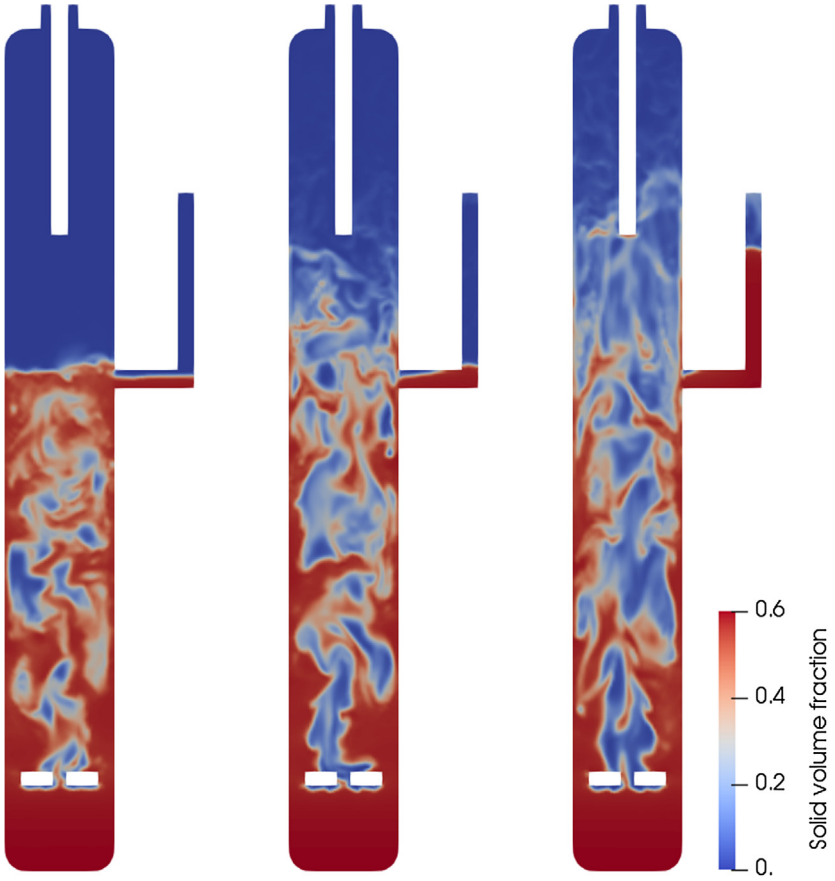

Fig. 9. Instantaneous solid volume fraction for different gas velocities. Left: $V_f = 0.3$ m/s, middle: $V_f = 0.6$ m/s and right: $V_f = 0.85$ m/s.

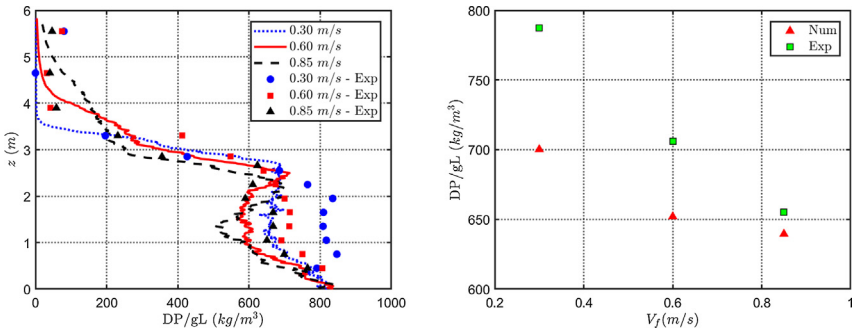

Fig. 10. Left: Profiles of mean vertical bed density for different gas velocities and right: average bed density in the dense region for different gas velocities.

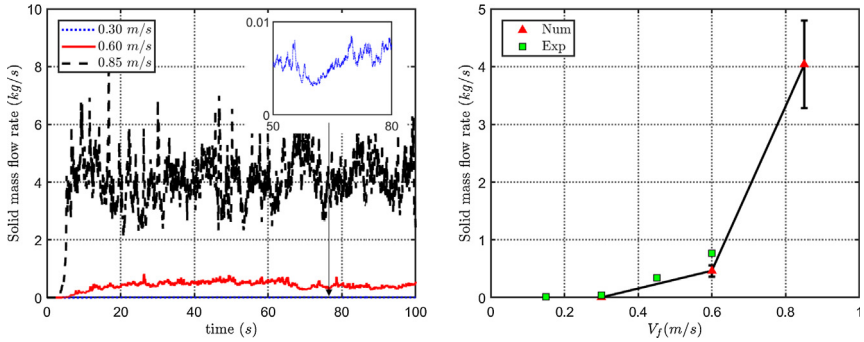

Fig. 11. Left: Solid mass flow rate at the outlet versus time (s) for different gas velocities and right: time-averaged solid mass flow rate compared to experimental data. The experimental point for $V_f = 0.85$ m/s was not available.

compared to the experimental result for the case $V_f = 0.6$ m/s. More importantly, an exponential augmentation of the solid mass flow rate is well captured when increasing superficial gas velocities. From $V_f = 0.3$ to 0.85 m/s, the flow regime changes from a turbulent fluidized bed to a quasi circulating fluidized bed, the recirculation rate is amplified by several orders of magnitude, from 10^{-3} to 10^{0} kg/s.

After these validations, some more details about results are given below.

6.2. Solid volume fraction

The mean solid volume fractions for different gas velocities are shown in Fig. 12. For all the three cases, high solid volume fraction is found in the near wall region and low solid volume fraction at the bed center. And it is obvious to see that there are two peaks of the solid volume fraction close to the wall, one is just above the air distributor, corresponding to the large number of particles blown up by the air, another one is located below the main cyclone dipleg, corresponding to particles going down by the gravity and by the return of the dipleg. Fig. 13 shows the radial profiles of time- and spatial-averaged solid volume fraction for different gas velocities at four horizontal planes. Generally, for the first three planes below the main cyclone dipleg ($z = 0.7$, 1.7 and 2.7 m), the profiles have a minimum at the center of the bed and a maximum at the wall for all the three cases. At the plane above the main cyclone dipleg $z = 3.7$ m, where is the transition zone between the dense region and the dilute region, the minimum is found not at the bed center but at $r/R \sim= 0.75$, except for the case with $V_f = 0.3$ m/s where rare particles can reach this height. Moreover, mean solid volume fraction decreases with the increase of the superficial gas velocity all along the radial direction at the first three planes.

6.3. Solid velocity

Fig. 14 shows the time- and spatial-averaged solid velocity field from the top of the air distributor to the bottom of the secondary cyclone dipleg for different gas velocities. The radial axis is amplified twice in order to see more clearly the velocity vectors. In general, particles move upwards at the center of the bed and downwards in the near wall region, and only one single clockwise macroscopic mixing loop of donut shape in 3D (Fede et al., 2016) is formed for all three gas velocities.

The radial profiles of the time- and spatial-averaged solid vertical velocity normalized by the superficial gas velocity are presented in Fig. 15. The profiles have a positive peak at the center of the bed and a negative minimum at the wall. From $z = 0.7$ to 2.7 m, particles move faster upwards at the bed center and downwards at the wall for all the three cases. At $z = 3.7$ m, particles are slowing down due to the effect of the gravity.

6.4. Solid mass flow rate

The mean solid mass flow rates normalized by the inlet gas mass flow rate at different horizontal planes are presented in Fig. 16. It can be clearly observed that solid particle flux goes upward through the bed center and goes downwards along the bed wall for all the three cases. The strongest gradient of the solid mass flow rate in the plane is found for the case $V_f = 0.3$ m/s, that corresponds to a dense fluidized bed for mixing, while the weakest gradient is found for the case $V_f = 0.85$ m/s corresponding to a circulating fluidized bed for particle transport.

Fig. 17 shows the radial profiles of time- and spatial-averaged solid mass flow rate normalized by the inlet gas mass flow rate at four horizontal planes. The positive solid mass flow rate at the bed center increases with the bed height from $z = 0.7$ to 2.7 m,

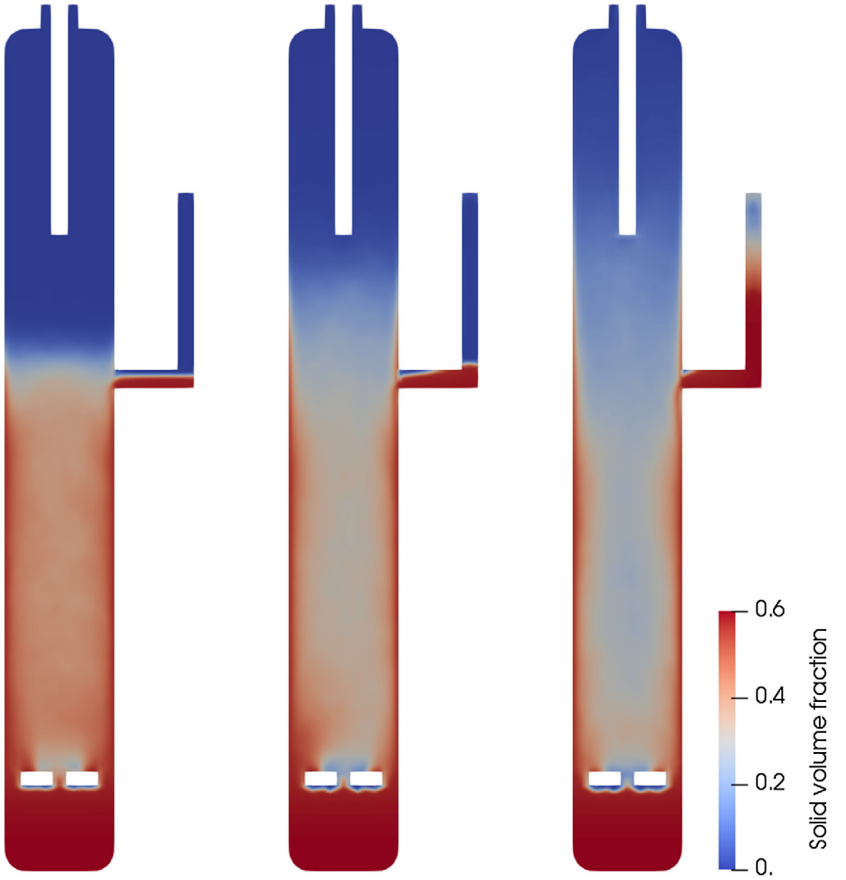

Fig. 12. Mean solid volume fraction for different gas velocities. Left: $V_f = 0.3$ m/s, middle: $V_f = 0.6$ m/s and right: $V_f = 0.85$ m/s.

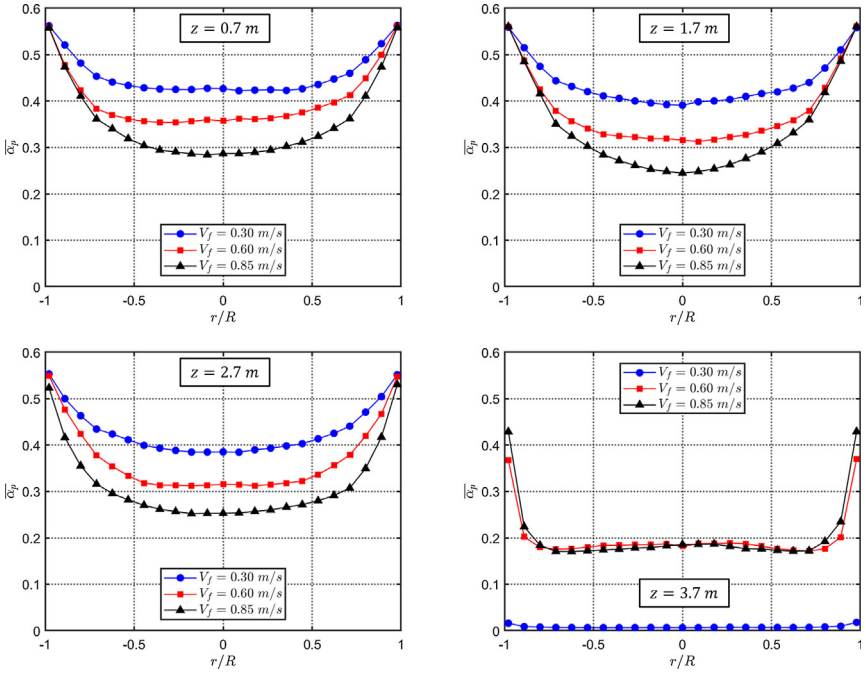

Fig. 13. Radial profiles of time- and spatial-averaged solid volume fraction for different gas velocities at four horizontal planes. Upper-left: $z = 0.7$ m, upper-right: $z = 1.7$ m, lower-left: $z = 2.7$ m and lower-right: $z = 3.7$ m.

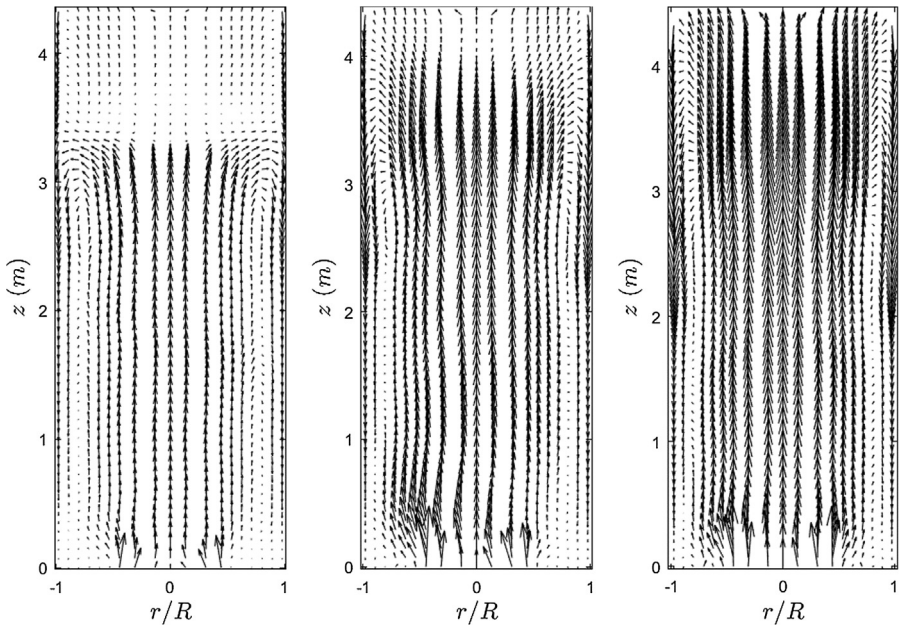

Fig. 14. Time- and spatial-averaged solid velocity field from the top of the air distributor to the bottom of the secondary cyclone dipleg for different gas velocities. Left: $V_f = 0.3$ m/s, middle: $V_f = 0.6$ m/s and right: $V_f = 0.85$ m/s.

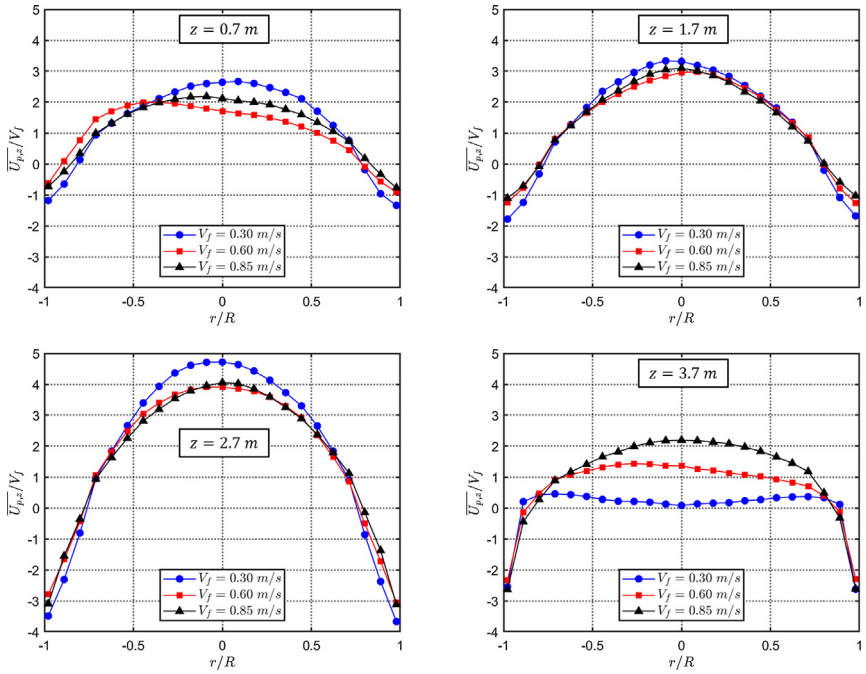

Fig. 15. Radial profiles of time- and spatial-averaged solid vertical velocity for different gas velocities at four horizontal planes. Upper-left: $z = 0.7$ m, upper-right: $z = 1.7$ m, lower-left: $z = 2.7$ m and lower-right: $z = 3.7$ m.

decreases at the highest plane. The same description can be used for the negative solid mass flow rate at the wall.

7. Conclusion

A CFD study of a large-scale fluidized bed is investigated using the NEPTUNE_CFD code based on an Eulerian n-fluid modeling approach. A major overestimation of the bed expansion is observed for the simulations on the coarse meshes which shows the necessity of using a SGS drag model. With the application of the SGS drag model developed by Ozel et al. (2013) without any specific or empirical tuning, reasonably good grid-independent results are obtained. The flow regimes inside the fluidized bed are well predicted for three different superficial gas velocities. The bed density profiles and the solid entrainment fluxes are also in good agreement with the experimental measurement. The validation of these simulations enhances the credibility of using such a SGS drag model and provides a feasibility for the further numerical study on industrial-scale fluidized bed.

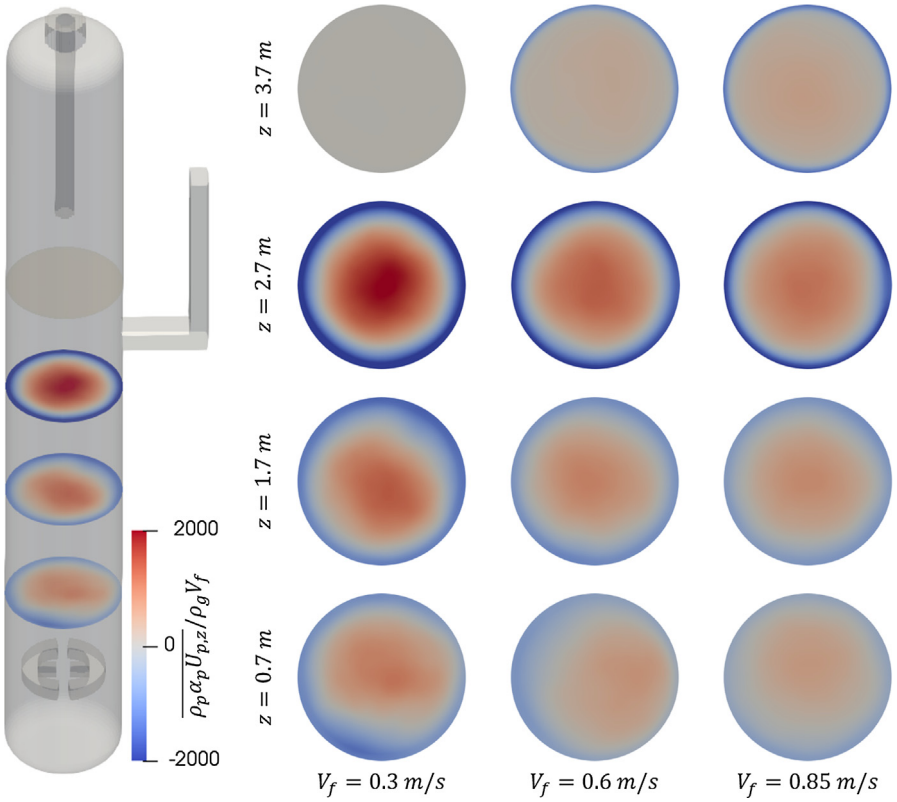

Fig. 16. Mean solid mass flow rate for different gas velocities at four horizontal planes along the bed height. Left: $V_f = 0.3$ m/s, middle: $V_f = 0.6$ m/s and right: $V_f = 0.85$ m/s.

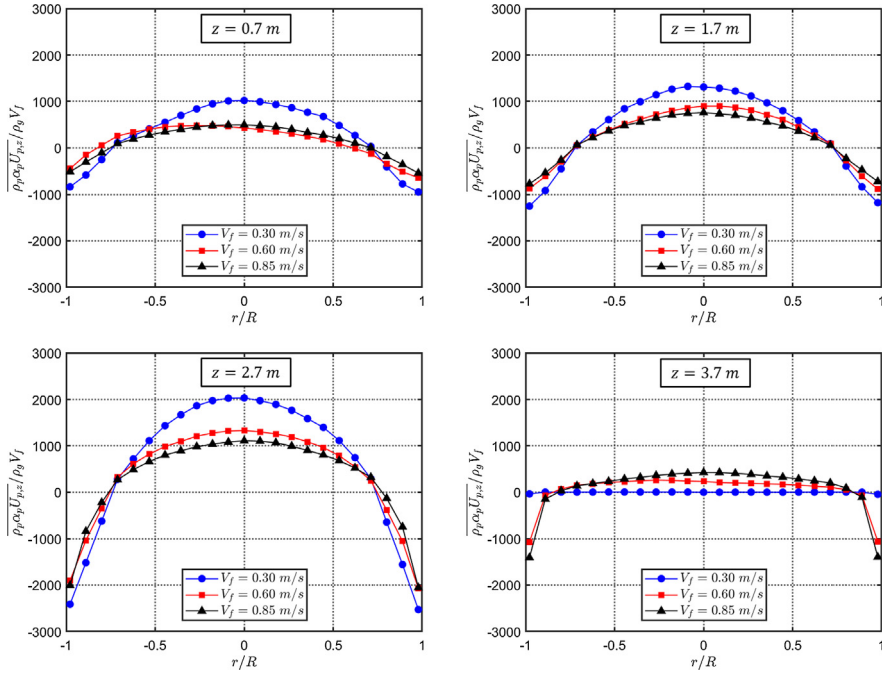

Fig. 17. Radial profiles of time- and spatial-averaged solid mass flow rate for different gas velocities at four horizontal planes. Upper-left: $z = 0.7$ m, upper-right: $z = 1.7$ m, lower-left: $z = 2.7$ m and lower-right: $z = 3.7$ m.

Declaration of Competing Interest

The authors declare that they have no known competing financial interests or personal relationships that could have appeared to influence the work reported in this paper.

Acknowledgments

This work was performed using HPC resources from CALMIP (Grant 2018 - p0111) and from CINES Occigen under the allocation $n^{\circ}A0022B06012$ and $n^{\circ}A0042B06012$. The authors are grateful to S. Sundaram, A. Issangya, B. Freireich, R. Cocco and S.B. Reddy Karri from Particulate Solid Research Inc. for sharing their experimental data in the 0.9 m diameter fluidized bed.

Appendix A. Derivation of filtered Euler-Euler two-phase model

In this appendix the set of the filtered equations of the multi-fluid Eulerian model is introduced. Hereafter, the gas phase corresponds to the subscript $k = g$ and the particulate phase to $k = p$.

Let $\alpha_k(\mathbf{x}, t)$ denote the volume fraction of phase k at location $\mathbf{x}$ and time t obtained by solving the Euler-Euler two-phase model equations. We can define the filtered phase volume fraction as

$$\overline{\alpha}_k(\mathbf{x}, t) = \iiint \alpha_k(\mathbf{r}, t) G(\mathbf{r} - \mathbf{x}) d\mathbf{r} \tag{A.1}$$

where $G(\mathbf{r} - \mathbf{x})$ is a weight function that satisfies $\iiint G(\mathbf{r} - \mathbf{x}) d\mathbf{r} = 1, \forall \mathbf{x}$. The filtered velocity of phase k is defined as

$$\widetilde{U}_k(\mathbf{x}, t) = \frac{1}{\overline{\alpha}_k} \iiint \alpha_k(\mathbf{r}, t) G(\mathbf{r} - \mathbf{x}) U_k(\mathbf{r}, t) d\mathbf{r} \tag{A.2}$$

Applying such a filter to the mass balance equation for the phase k, we obtain

$$\frac{\partial}{\partial t} \rho_k \overline{\alpha}_k + \frac{\partial}{\partial x_j} \rho_k \overline{\alpha}_k \widetilde{U}_{k,j} = 0 \tag{A.3}$$

This filtering procedure can be applied to momentum balance equation for the phase k, we have

$$\begin{aligned} \tfrac{\partial}{\partial t} \rho_k \overline{\alpha}_k \widetilde{U}_{k,i} + \tfrac{\partial}{\partial x_j} \rho_k \overline{\alpha}_k \widetilde{U}_{k,i} \widetilde{U}_{k,j} \quad &= \rho_k \overline{\alpha}_k g_i - \overline{\alpha}_k \tfrac{\partial \overline{p}_g}{\partial x_i} - \varphi^{sgs}_{k,i} \\ &+ \widetilde{I}_{k,i} + I^{sgs}_{k,i} - \tfrac{\partial}{\partial x_j} \widetilde{\Sigma}_{k,ij} - \tfrac{\partial}{\partial x_j} \Sigma^{sgs}_{k,ij} \\ &- \tfrac{\partial}{\partial x_j} \rho_k \overline{\alpha}_k \sigma^{sgs}_{k,ij} \end{aligned} \tag{A.4}$$

Terms with superscript (^{sgs}) in Eq. (A.4) appear from the filtering process and they represent the interaction between resolved and subgrid contributions. The first term on the right is the gravity contribution. The second line is the resolved and subgrid buoyancy force. The third line shows the resolved and subgrid drag force. The fourth line is the resolved and subgrid stress tensor. The last terms is a Reynolds stress-like contribution coming from the fluctuation velocity of phase k. Thus, four subgrid terms have to be closed. According to the budget analysis in Parmentier et al. (2012) and Ozel et al. (2013), the subgrid drag force has a dominant effect on the prediction of the bed expansion. Therefore, in the actual study, we focus on the modeling of the subgrid drag force term $I^{sgs}_{k,i}$ and choose to neglect three other contributions. The drag force terms $\widetilde{I}_{k,i}$ and $I^{sgs}_{k,i}$ are defined as

$$\widetilde{I}_{g,i} = -\widetilde{I}_{p,i} = \frac{\rho_p \overline{\alpha}_p}{\widetilde{\tau}^F_{gp}} \left(\widetilde{U}_{p,i} - \widetilde{U}_{g,i} \right) \tag{A.5}$$

$$I^{sgs}_{g,i} = -I^{sgs}_{p,i} = \overline{\frac{\rho_p \alpha_p}{\tau^F_{gp}} V_{r,i}} - \frac{\rho_p \overline{\alpha}_p}{\widetilde{\tau}^F_{gp}} \left(\widetilde{U}_{p,i} - \widetilde{U}_{g,i} \right) \tag{A.6}$$

where $V_{r,i} = U_{p,i} - U_{g,i}$ is the relative velocity, τ^F_{gp} is the mean particle relaxation time. The filtered drag force can be approximated by

$$\overline{\frac{\rho_p \alpha_p}{\tau^F_{gp}} V_{r,i}} \simeq \frac{\rho_p}{\widetilde{\tau}^F_{gp}} \overline{\alpha_p V_{r,i}} \tag{A.7}$$

where $\overline{\alpha_p V_{r,i}} = \overline{\alpha}_p \left(\widetilde{U}_{p,i} - \widetilde{U}_{g@p,i} \right)$. By introducing a subgrid drift velocity $\widetilde{V}_{d,i}$ which is defined as the difference between the filtered gas velocity seen by the particle phase and the filtered gas velocity seen by the gas phase, $\widetilde{V}_{d,i} = \widetilde{U}_{g@p,i} - \widetilde{U}_{g,i}$, Eq. (A.6) becomes

$$I^{sgs}_{g,i} = -I^{sgs}_{p,i} = -\frac{\rho_p \overline{\alpha}_p}{\widetilde{\tau}^F_{gp}} \widetilde{V}_{d,i} \tag{A.8}$$

According to Parmentier et al. (2012), $\widetilde{V}_{d,i}$ can be modeled by:

$$\widetilde{V}_{d,i} = -g(\overline{\Delta}, \overline{\alpha}_p) K_{ij} \left(\widetilde{U}_{p,j} - \widetilde{U}_{g,j} \right) \tag{A.9}$$

where $g(\overline{\Delta}, \overline{\alpha}_p)$ is a function of the filter size $\overline{\Delta}$ and filtered particle volume fraction $\overline{\alpha}_p$, it can be approximated by a multiplication of two independent functions $f(\overline{\Delta})$ and $h(\overline{\alpha}_p)$. K_{ij} is a second order symmetric tensor. It is assumed that $K_{xy} = K_{yz} = K_{xz} = 0$ and $K_{xx} = K_{yy}$ for the three-dimensional fluidized bed simulations where the gravity is in the z-direction. Thus, $\widetilde{V}_{d,i}$ can be evaluated by

$$\widetilde{V}_{d,\beta} = -K_{\beta\beta} f(\overline{\Delta}) h(\overline{\alpha}_p) \left(\widetilde{U}_{p,\beta} - \widetilde{U}_{g,\beta} \right) \tag{A.10}$$

where the Greek subscript $\beta = x, y, z$ and is used to indicate that there is no implicit summation. The constant $K_{\beta\beta}$ is dynamically adjusted by a procedure detailed in Appendix B. $h(\overline{\alpha}_p)$ is measured from fine-grid simulations and given as

$$h(\overline{\alpha}_p) = -tanh\left(\frac{\overline{\alpha}_p}{0.1} \right) \sqrt{\frac{\overline{\alpha}_p}{0.64}} \left(1 - \frac{\overline{\alpha}_p}{0.64} \right)^2 \quad 1 - 1.88 \frac{\overline{\alpha}_p}{0.64} + 5.16 \left(\frac{\overline{\alpha}_p}{0.64} \right)^2 \tag{A.11}$$

The following form is proposed for $f(\overline{\Delta})$,

$$f(\overline{\Delta}) = \frac{\overline{\Delta}^2}{\overline{\Delta}^2 + C} \tag{A.12}$$

where $C = 0.15 \left(\widetilde{\tau}^F_{gp} \left| \widetilde{V}_r \right| \right)^2$, $|\widetilde{V}_r|$ is the magnitude of the filtered relative velocity. To summarize, the filtered drag force is modeled by:

$$\overline{\frac{\rho_p \alpha_p}{\tau^F_{gp}} V_{r,\beta}} = \frac{\rho_p \overline{\alpha}_p}{\widetilde{\tau}^F_{gp}} \left(1 + K_{\beta\beta} f(\overline{\Delta}) h(\overline{\alpha}_p) \right) \left(\widetilde{U}_{p,\beta} - \widetilde{U}_{g,\beta} \right) \tag{A.13}$$

It should be noted that a clipping is applied to $K_{\beta\beta} f(\overline{\Delta}) h(\overline{\alpha}_p)$ in these simulations in order to remove those values lower than -0.99999, avoiding a filtered drag force in the direction opposite to its resolved part.

Appendix B. Dynamic adjustment of the model constant $K_{\beta\beta}$

Parmentier et al. (2012) proposed adjusting the model constants $K_{\beta\beta}$ dynamically by using a method adapted from Germano et al. (1991) and Lilly (1992). The constant are dependent on both the case simulated and the direction. The idea is to estimate values of $K_{\beta\beta}$ for each cell during the simulation on a coarse grid, by performing a filtering operation of variables over cells in the neighborhood. Test-level filtered function $\hat{\overline{f}}$ can be averaged over the base level function $\overline{f}$ for a uniform 3D mesh

$$\begin{aligned}\hat{\overline{f}}(\mathbf{x},t) &= \tfrac{1}{7}\Big(\overline{f}(\mathbf{x},t)+\overline{f}\Big(\mathbf{x}+\widehat{\Delta}\mathbf{e}_{\mathbf{x}},t\Big)+\overline{f}\Big(\mathbf{x}-\widehat{\Delta}\mathbf{e}_{\mathbf{x}},t\Big)+\overline{f}\Big(\mathbf{x}+\widehat{\Delta}\mathbf{e}_{\mathbf{y}},t\Big)\\ &\quad+\overline{f}\Big(\mathbf{x}-\widehat{\Delta}\mathbf{e}_{\mathbf{y}},t\Big)+\overline{f}\Big(\mathbf{x}+\widehat{\Delta}\mathbf{e}_{\mathbf{z}},t\Big)+\overline{f}\Big(\mathbf{x}-\widehat{\Delta}\mathbf{e}_{\mathbf{z}},t\Big)\Big)\end{aligned} \tag{B.1}$$

where $\widehat{\Delta}$ is the test-level filter width. Parmentier et al. (2012) tested the function $f(\overline{\Delta}),g(\overline{\alpha}_p)$ at the test and the base filter levels. They state the both functions are nearly independent of the choice of the filter width. The model at the base level is given by:

$$\begin{aligned}\overline{\alpha}_p\widetilde{V}_{d,\beta} &= -\overline{\alpha_p\left(U_{p,\beta}-U_{g,\beta}\right)}+\overline{\alpha}_p\left(\widetilde{U}_{p,\beta}-\widetilde{U}_{g,\beta}\right)\\ &= -\overline{\alpha}_pK_{\beta\beta}f(\overline{\Delta})h(\overline{\alpha}_p)\left(\widetilde{U}_{p,\beta}-\widetilde{U}_{g,\beta}\right)\end{aligned} \tag{B.2}$$

Consequently, one can define the subgrid drift velocity $\mathcal{T}_\beta$ at test scale obeying the same modeling assumption as

$$\begin{aligned}\mathcal{T}_\beta &= -\widehat{\overline{\alpha_p\left(U_{p,\beta}-U_{g,\beta}\right)}}+\widehat{\overline{\alpha}}_p\left(\widehat{\widetilde{U}}_{p,\beta}-\widehat{\widetilde{U}}_{g,\beta}\right)\\ &= -\widehat{\overline{\alpha}}_pK_{\beta\beta}f\left(\widehat{\Delta}\right)h\left(\widehat{\overline{\alpha}}_p\right)\left(\widehat{\widetilde{U}}_{p,\beta}-\widehat{\widetilde{U}}_{g,\beta}\right)\end{aligned} \tag{B.3}$$

The filtered subgrid drift velocity is given by:

$$\mathcal{F}_\beta=\widehat{\overline{\alpha}_p\widetilde{V}_{d,\beta}}=-\widehat{\overline{\alpha_p\left(U_{p,\beta}-U_{g,\beta}\right)}}+\overline{\alpha}_p\left(\widehat{\widetilde{U}_{p,\beta}}-\widetilde{U}_{g,\beta}\right) \tag{B.4}$$

The difference between the filtered subgrid drift velocity (Eq. (B.4)) and the subgrid drift velocity at the test scale (Eq. (B.3)) is

$$\mathcal{L}_\beta=\mathcal{F}_\beta-\mathcal{T}_\beta=\overline{\alpha}_p\left(\widehat{\widetilde{U}_{p,\beta}}-\widetilde{U}_{g,\beta}\right)-\widehat{\overline{\alpha}}_p\left(\widehat{\widetilde{U}}_{p,\beta}-\widehat{\widetilde{U}}_{g,\beta}\right) \tag{B.5}$$

Moreover, assuming that the variation of $K_{\beta\beta}$ is negligible between two different scale levels, substitution of Eq. (B.2) and Eq. (B.3) into Eq. (B.5) leads to the following relations:

$$\mathcal{L}_\beta=-K_{\beta\beta}\mathcal{M}_\beta \tag{B.6}$$

where

$$\mathcal{M}_\beta=f(\overline{\Delta})h(\overline{\alpha}_p)\widehat{\overline{\alpha}_p\left(\widetilde{U}_{p,\beta}-\widetilde{U}_{g,\beta}\right)}-f\left(\widehat{\Delta}\right)h\left(\widehat{\overline{\alpha}}_p\right)\widehat{\overline{\alpha}}_p\left(\widehat{\widetilde{U}}_{p,\beta}-\widehat{\widetilde{U}}_{g,\beta}\right).$$

Thus, we can obtain a model coefficient as

$$K_{\beta\beta}\approx-\frac{\mathcal{L}_\beta}{\mathcal{M}_\beta} \tag{B.7}$$

For three-dimensional simulations, the model coefficients along x- and y-directions are assumed to be the same and given by following relation:

$$K_{xx}=K_{yy}=-\frac{\mathcal{L}_x\mathcal{M}_x+\mathcal{L}_y\mathcal{M}_y}{\mathcal{M}_x^2+\mathcal{M}_y^2} \tag{B.8}$$

References

Agrawal, Kapil, Loezos, Peter N., Syamlal, Madhava, Sundaresan, Sankaran, 2001. The role of meso-scale structures in rapid gas–solid flows. J. Fluid Mech. 445, 151–185.

Amblard, Benjamin, Singh, Raj, Gbordzoe, Eusebius, Raynal, Ludovic, 2017. CFD modeling of the coke combustion in an industrial FCC regenerator. Chem. Eng. Sci. 170, 731–742.

Andrews, Arthur T., Loezos, Peter N., Sundaresan, Sankaran, 2005. Coarse-Grid Simulation of Gas-Particle Flows in Vertical Risers. Ind. Eng. Chem. Res. 44 (16), 6022–6037.

Bennani, L., Neau, H., Baudry, C., Laviéville, J., Fede, P., Simonin, O., 2017. Numerical simulation of unsteady dense granular flows with rotating geometries. Chem. Eng. Res. Des. 120, 333–347.

Cloete, Jan Hendrik, Cloete, Schalk, Municchi, Federico, Radl, Stefan, Amini, Shahriar, 2018a. Development and verification of anisotropic drag closures for filtered Two Fluid Models. Chem. Eng. Sci. 192, 930–954.

Cloete, Jan Hendrik, Cloete, Schalk, Radl, Stefan, Amini, Shahriar, 2018b. Development and verification of anisotropic solids stress closures for filtered Two Fluid Models. Chem. Eng. Sci. 192, 906–929.

Ergun, Sabri, 1952. Fluid flow through packed columns. Chem. Eng. Prog. 48 (2), 89–94.

Fede, Pascal, Simonin, Olivier, Ingram, Andrew, 2016. 3D numerical simulation of a lab-scale pressurized dense fluidized bed focussing on the effect of the particle-particle restitution coefficient and particle–wall boundary conditions. Chem. Eng. Sci. 142, 215–235.

Fullmer, William D., Hrenya, Christine M., 2017. The clustering instability in rapid granular and gas-solid flows. Annu. Rev. Fluid Mech. 49 (1), 485–510.

Germano, Massimo, Piomelli, Ugo, Moin, Parviz, Cabot, William H., 1991. A dynamic subgrid-scale eddy viscosity model. Phys. Fluids A 3 (7), 1760–1765.

Gobin, Anne, Neau, Hervé, Simonin, Olivier, Llinas, Jean-Richard, Reiling, Vince, Sélo, Jean-Lof, 2003. Fluid dynamic numerical simulation of a gas phase polymerization reactor. Int. J. Numer. Meth. Fluids 43 (10–11), 1199–1220.

Igci, Yesim, Sundaresan, Sankaran, 2011a. Verification of filtered two-fluid models for gas-particle flows in risers. AIChE J. 57 (10), 2691–2707.

Igci, Yesim, Sundaresan, Sankaran, 2011b. Constitutive models for filtered two-fluid models of fluidized gas-particle flows. Ind. Eng. Chem. Res. 50 (23), 13190–13201.

Hamidouche, Z., Masi, E., Fede, P., Ansart, R., Neau, H., Hemati, M., Simonin, O., 2018. Numerical simulation of multiphase reactive flows. Part I, Alessandro Parente and Juray De, 1st ed., 52. Wilde, Academic Press, pp. 55–121.

Igci, Yesim, Andrews, Arthur T., Sundaresan, Sankaran, Pannala, Sreekanth, O'Brien, Thomas, 2008. Filtered two-fluid models for fluidized gas-particle suspensions. AIChE J. 54 (6), 1431–1448.

Li, Jinghai, Kwauk, Mooson, 1994. Particle-Fluid Two-Phase Flow: The Energy-Minimization Multi-Scale Method. Metallurgical Industry Press, Beijing.

Li, Jinghai, Kwauk, Mooson, 2003. Exploring complex systems in chemical engineering—the multi-scale methodology. Chem. Eng. Sci. 58 (3), 521–535.

Li, J., Ge, W., Zhang, J., Gao, S., Wang, W., Yang, N., Sun, Q., Gao, J., 2007. Analytical multi-scale methodology for fluidization systems - retrospect and prospect, The 12th International Conference on Fluidization - New Horizons in Fluidization Engineering.

Lilly, D.K., 1992. A proposed modification of the Germano subgrid-scale closure method. Phys. Fluids A 4 (3), 633–635.

Milioli, Christian C., Milioli, Fernando E., Holloway, William, Agrawal, Kapil, Sundaresan, Sankaran, 2013. Filtered two-fluid models of fluidized gas-particle flows: New constitutive relations. AIChE J. 59 (9), 3265–3275.

Ozel, A., Fede, P., Simonin, O., 2013. Development of filtered Euler-Euler two-phase model for circulating fluidised bed: High resolution simulation, formulation and a priori analyses. Int. J. Multiph. Flow 55, 43–63.

Parmentier, Jean-François, Simonin, Olivier, Delsart, Olivier, 2012. A functional subgrid drift velocity model for filtered drag prediction in dense fluidized bed. AIChE J. 58 (4), 1084–1098.

Sarkar, Avik, Milioli, Fernando E., Ozarkar, Shailesh, Li, Tingwen, Sun, Xin, Sundaresan, Sankaran, 2016. Filtered sub-grid constitutive models for fluidized gas-particle flows constructed from 3-D simulations. Chem. Eng. Sci. 152, 443–456.

Schneiderbauer, Simon, 2017. A spatially-averaged two-fluid model for dense large-scale gas-solid flows. AIChE J. 63 (8), 3544–3562.

Schneiderbauer, Simon, Pirker, Stefan, 2014. Filtered and heterogeneity-based subgrid modifications for gas–solid drag and solid stresses in bubbling fluidized beds. AIChE J. 60 (3), 839–854.

Schneiderbauer, Simon, Puttinger, Stefan, Pirker, Stefan, 2013. Comparative analysis of subgrid drag modifications for dense gas-particle flows in bubbling fluidized beds. AIChE J. 59 (11), 4077–4099.

Simonin, O., 2000. Statistical and continuum modelling of turbulent reactive particulate flows. Rhode Saint Genèse. Lecture Series, 6. von Karman Institute for Fluid Dynamics, Belgium.

Simonin, Olivier, Février, Pierre, Laviéville, Jérôme, 2002. On the spatial distribution of heavy-particle velocities in turbulent flow: From continuous field to particulate chaos. J. Turbul. 3.

Srivastava, Anuj, Sundaresan, Sankaran, 2003. Analysis of a frictional–kinetic model for gas–particle flow. Powder Technol. 129 (1), 72–85.

Sundaresan, Sankaran, Ozel, Ali, Kolehmainen, Jari, 2018. Toward constitutive models for momentum, species, and energy transport in gas-particle flows. Annual Rev. Chem. Biomol. Eng. 9 (1), 61–81.

van der Hoef, M.A., van Sint Annaland, M., Deen, N.G., Kuipers, J.A.M., 2008. Numerical simulation of dense gas-solid fluidized beds: A multiscale modeling strategy. Annu. Rev. Fluid Mech. 40 (1), 47–70.

Wang, Junwu, 2009. A review of Eulerian simulation of Geldart a particles in gas-fluidized beds. Ind. Eng. Chem. Res. 48 (12), 5567–5577.

Wang, Junwu, Ge, Wei, Li, Jinghai, 2008. Eulerian simulation of heterogeneous gas–solid flows in CFB risers: EMMS-based sub-grid scale model with a revised cluster description. Chem. Eng. Sci. 63 (6), 1553–1571.

Wen, C.Y., Yu, Y.H., 1965. Mechanics of Fluidization. Chem. Eng. Progress Symp. Ser. 62, 100–111.